Mode expansion modeling of rectangular integrated optical microresonators

M A N F R E D   L O H M E Y E R
*Faculty of Mathematical Sciences, MESA+ Research Institute, University of Twente, P.O. Box 217, 7500
AE Enschede, The Netherlands (E-mail: m.lohmeyer@math.utwente.nl)*

Abstract. Two dielectric waveguides that are evanescently coupled to a square or rectangular region of increased refractive index can serve as a very compact integrated optical microresonator. We consider these devices in a spatial two-dimensional setting, where a rigorous mode expansion technique enables accurate and quite efficient numerical simulations of these configurations. The paper is concerned with single resonator units as well as with an add-drop filter constructed by cascading two square cavities. Besides calculating the power transmission spectra, we try to document as far as possible the characteristic electric field patterns that occur at major and minor resonance wavelengths. The influence of the various geometrical parameters on the resonator performance is investigated in detail.

Key words: add-drop-filter, integrated optics, microresonator, numerical modeling, wavelength demultiplexing

1. Introduction

Compact integrated optical microresonator devices are currently discussed as one of the most promising concepts for applications in optical wavelength division multiplexing. A typical resonator element includes two parallel dielectric waveguides, serving as input- and output-ports, which are connected by a small optical cavity in between. Depending on the precise configuration, the resonator can exhibit excellent wavelength add-drop characteristics. A technique that employs microresonators for wavelength demultiplexing in an integrated optical setting could eventually constitute an alternative to well established conventional approaches such as arrayed waveguide gratings, where the typical device dimensions are considerably larger.

Traditionally (Marcatili 1969) the majority of microresonator proposals deals with smooth cylindrical or spherical geometries (see e.g. Rowland and Love 1993; Chin and Ho 1997; Little *et al.* 1997, 1999; Boriskina and Nosich 1999 and references cited therein), where recently the optical properties of elliptical cavities have attracted some attention (Nöckel and Stone 1997; Gornik 1998). Alternatively, coupling the port waveguides by small square or rectangular cavities can also lead to resonator devices that show the desired filter functionality. Such a configuration has been proposed by Manolatou

et al. (1999). Poon *et al.* (2001) collects some experimental results regarding the spectral properties of rectangular cavities.

Apart from proper performance and extreme compactness, a square resonator unit as considered in Fig. 1 has the nice property that it can be simulated quite efficiently by well established mode decomposition techniques (Vassallo 1991; Sztefka and Nolting 1993; Lohmeyer and Stoffer 2001), provided that these are adapted to the specific properties of the resonator. We consider the structure as being composed of three longitudinally homogeneous waveguide segments. For fixed frequency, the electromagnetic field is expanded into the local modes of the segments, including propagating and evanescent, forwards and backwards directed terms. Matching adjacent fields at the segment boundaries yields the transmission characteristics of the device.

Section 2 briefly surveys the mode expansion approach. Subsequently, Section 3 gives a detailed account of the simulation results for single rectangular resonators, including several illustrations of the standing wave field patterns for some of the resonant configurations. The section closes with a few remarks on the convergence behavior of the simulation technique. While a single almost square unit drops equal amounts of power into all four ports at the resonance wavelength, proper add-drop filter performance can be achieved by employing two equal cavities at a specific distance (Manolatou *et al.* 1999). Section 4 reports on our simulations of the filter device.
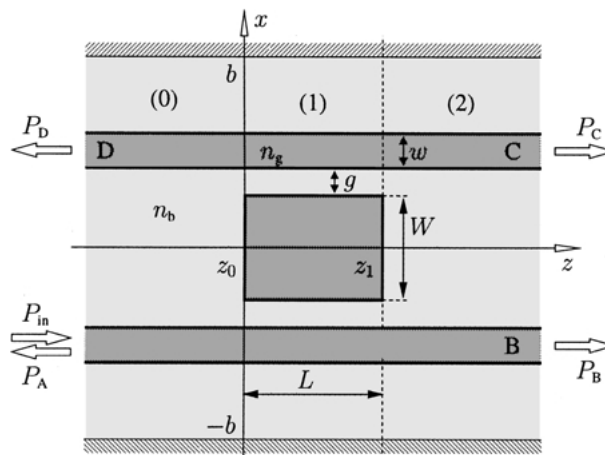

Fig. 1. The microresonator configuration. z and x are the Cartesian coordinate axes parallel and perpendicular to the waveguides. The geometry is fixed in terms of the width w of the waveguides, the gap width g, and the width W and length L of the cavity. n_b and n_g are the refractive indices of the background and the guiding regions ($n_b < n_g$), where the latter are indicated by darker shading. The letters A, B, C, and D denote the input and output ports, where the light is assumed to enter the structure via the guided mode of port A. The numbers (0) to (2) identify three longitudinally (z-) homogeneous sections, separated by the two junctions at $z_0 = 0$ and $z_1 = L$. Artificial boundaries are placed at $x = \pm b$.

2. Rigorous mode expansion modeling

The microresonator configuration of Fig. 1 is to be investigated, in a two-dimensional (2D) setting of spatial coordinates x and z, with the structure meant to be symmetric with respect to the lines $x = 0$ and $z = L/2$. The fixed angular light frequency ω will be specified in terms of the vacuum wavelength $\lambda = 2\pi/k = 2\pi c/\omega$, where k and c are the vacuum wavenumber and the vacuum speed of light. Evaluating the spectral response of the device requires a sequence of calculations for varying vacuum wavelength.

The mode expansion simulation starts with a division of the structure into $N + 2$ segments with longitudinally homogeneous permittivity profile, identified by a cipher in parentheses. N is the number of inner segments, $N = 1$ for the example of Fig. 1. The segment junctions are located at $z_0, \ldots, z_N$.

We introduce artificial boundaries at positions $x = \pm b$, where the basic components of all involved mode fields are assumed to vanish. b is understood to be large when compared to the x-dimensions of the resonator structure. These boundaries lead to a discretization of the mode spectra of the waveguide segments; the mode sets become numerically manageable. At the same time, the hard boundary conditions cause radiated parts of the electromagnetic field to be backreflected at the lines $x = \pm b$ into the computational domain. Nevertheless we regard this procedure to be admissible for the present problems. The structures are to be excited by a well localized input in one of the port waveguides, and the scattering part of the devices is relatively short (this refers to the z-extension) when compared to the width $2b$ of the computational window, such that the optical power radiated at one of the junctions is unlikely to reenter the structure within an inner segment. Apart from the port waveguides, we are interested in the electromagnetic field only in a small region around the cavity. Hence the approximation caused by the artificial boundaries should be admissible, if the walls are placed far enough away from the resonator region. This also implies that b is large when compared to the extension of the guided input/output mode profile.

Separately for each segment (s), the total electromagnetic field $\mathscr{E}$, $\mathscr{H}$ (in common complex notation) is then expanded into a mode superposition of the form

$$\begin{pmatrix} \mathscr{E} \\ \mathscr{H} \end{pmatrix}^s (x,z,t) = \sum_m f_m^s \psi_m^{s,\mathrm{f}}(x) \exp(\mathrm{i}\omega t - \mathrm{i}\beta_m^s(z - z_{s-1}))$$
$$+ \sum_m b_m^s \psi_m^{s,\mathrm{b}}(x) \exp(\mathrm{i}\omega t + \mathrm{i}\beta_m^s(z - z_{s-1})). \tag{1}$$

Here $\psi_m^{s,d}$ combines the electric and magnetic parts of the forwards ($d = \mathrm{f}$) and backwards ($d = \mathrm{b}$) traveling versions of the profile of mode m on segment (s); β_m^s are the corresponding propagation constants. The constant

mode amplitudes f_m^s, b_m^s include the mode normalization. The junction positions were introduced as local coordinate offsets (with $z_{-1} = z_0$).

For the simulation of the resonator structures, the set of basis modes has to consist of forwards and backwards traveling, propagating and evanescent terms. While a detailed account on the notation used here, on the properties of the mode fields, and on the relevant orthogonality relations can be found elsewhere (Lohmeyer and Stoffer 2001), special attention has to be paid to the composition of the mode set e.g. on the entry and exit segments (0) and (2) in Fig. 1, where two distant parallel single mode waveguides are present. The two lowest order modes of this bounded refractive index profile correspond to the symmetric and antisymmetric superposition ('supermodes') of the guided fields of the two separate waveguides. Due to the large waveguide separation, these modes are numerically exactly degenerate, thus not directly identifiable by a mode solver that relies on a propagation constant search procedure. Here one might think of splitting the computational window at $x = 0$ and introducing boundary conditions that enforce separately modal solutions with either even or odd symmetry. In both – then decoupled – sets of modes one solution should show up that corresponds to the confined fields of the port waveguides, thus enabling the assembly of the supermodes with both symmetries.

Alternatively, we have constructed the mode set by using the modes of the bound structure with propagation constants below kn_b up to a certain order, together with two times the guided mode profile of an open single waveguide configuration, shifted to the actual positions of the waveguides. Provided that the waveguide separation and the computational window are large when compared to the width of the guided fields, this procedure results in a numerically exactly orthogonal basis set. After reserving the index 0 for the mode corresponding to the guided field of the lower waveguide and the index 1 for the upper one, this formulation allows to directly access the optical input power as $P_{in} = |f_0^0|^2 P_0^0$, and the power dropped into ports A to D as

$$P_A = |b_0^0|^2 P_0^0, \quad P_B = |f_0^{N+1}|^2 P_0^{N+1}, \quad P_C = |f_1^{N+1}|^2 P_1^{N+1}, \quad P_D = |b_1^0|^2 P_1^0.$$

$$(2)$$

Here P_m^s is the mode power assigned to basis field m on segment s (see Lohmeyer and Stoffer 2001).

The local mode amplitudes at the left end (z_{s-1}, index l) and at the right end (z_s, index r) of segment (s) are combined into amplitude vectors

$$\boldsymbol{f}_l^s = (f_m^s), \quad \boldsymbol{b}_l^s = (b_m^s), \quad \boldsymbol{f}_r^s = (f_m^s \exp(i\beta_m^s(z_s - z_{s-1}))),$$
$$\boldsymbol{b}_r^s = (b_m^s \exp(-i\beta_m^s(z_s - z_{s-1}))).$$

Now by bidirectional projection of the adjacent fields at the junctions onto the orthogonal basis sets one finds the amplitude vectors on either side of the junction at z_{j-1} connected as

$$
\begin{pmatrix} f_r^{j-1} \\ b_r^{j-1} \end{pmatrix} = \begin{pmatrix} M_{ff}^{j,-} & M_{fb}^{j,-} \\ M_{bf}^{j,-} & M_{bb}^{j,-} \end{pmatrix} \begin{pmatrix} f_1^j \\ b_1^j \end{pmatrix}, \quad \begin{pmatrix} f_1^j \\ b_1^j \end{pmatrix} = \begin{pmatrix} M_{ff}^{j,+} & M_{fb}^{j,+} \\ M_{bf}^{j,+} & M_{bb}^{j,+} \end{pmatrix} \begin{pmatrix} f_r^{j-1} \\ b_r^{j-1} \end{pmatrix}.
$$

(4)

The matrices $M^{j,\pm}$, $j = 1, \ldots, N + 1$, collect the mode overlaps at the segment junctions, (Lohmeyer and Stoffer 2001) for the precise definition. While necessarily the entries of $M^{j,-}$ and $M^{j,+}$ are related, these relations need not to be used when deriving the algorithm given by Equations (6)–(8) below. The light propagation inside the segments (s) is described by matrices $T_\pm^s s, = 1, \ldots, N$, that include the phase velocities respectively attenuation factors of the involved modes:

$$
\begin{aligned}
f_r^s &= T_+^s f_1^s, \quad b_r^s = T_-^s b_1^s, \\
f_1^s &= T_-^s f_r^s, \quad b_1^s = T_+^s b_r^s,
\end{aligned}
\quad \text{where } (T_\pm^s)_{lm} = \begin{cases} \exp(\mp i\beta_m^s(z_s - z_{s-1})), & \text{if } l = m, \\ 0 & \text{otherwise.} \end{cases}
$$

(5)

The system of Equations (4) and (5) is twofold overdetermined. Assuming that for a large number of terms in the mode expansions the two matrices in Equation (4) become equivalent, appropriate equations may be selected. Here we have to observe a numerical constraint: due to the exponential z-dependence of the evanescent modes in the basis set (with imaginary propagation constants $\beta = -i\alpha$, $\alpha > 0$), one should avoid the direct application of T_-^s in the numerical implementation. The following recipe complies to that requirement.

Given $f_r^0 = ((P_{in}/P_0^0)^{1/2}, 0, \ldots, 0)$ and $b_1^{N+1} = 0$ as a right hand side, Equations (4) and (5) are to be solved for all other unknown mode amplitudes. Starting with defining R^N as

$$
R^N = \left(1 - M_{bf}^{N+1,-} M_{fb}^{N+1,+}\right)^{-1} M_{bf}^{N+1,-} M_{ff}^{N+1,+},
$$

(6)

a sequence of reflection matrices R^j can be built iteratively

$$
R^{j-1} = \left(1 - \left(M_{bf}^{j,-} + M_{bb}^{j,-} T_+^j R^j T_+^j\right) M_{fb}^{j,+}\right)^{-1} \left(M_{bf}^{j,-} + M_{bb}^{j,-} T_+^j R^j T_+^j\right) M_{ff}^{j,+}
$$

(7)

that relate forward and backward mode amplitudes on the left side of the corresponding junctions. Arriving at R^0, the field amplitudes are readily obtained by subsequent backsubstitution:

$$\boldsymbol{b}_{\mathrm{r}}^{0} = \mathrm{R}^{0}\boldsymbol{f}_{r}^{0},$$
$$\boldsymbol{f}_{1}^{s} = \mathrm{M}_{\mathrm{ff}}^{s,+}\boldsymbol{f}_{\mathrm{r}}^{s-1} + \mathrm{M}_{\mathrm{fb}}^{s,+}\boldsymbol{b}_{\mathrm{r}}^{s-1},$$
$$\boldsymbol{f}_{\mathrm{r}}^{s} = \mathrm{T}_{+}^{s}\boldsymbol{f}_{1}^{s}, \quad \boldsymbol{b}_{\mathrm{r}}^{s} = \mathrm{R}^{s}\boldsymbol{f}_{\mathrm{r}}^{s}, \quad \boldsymbol{b}_{1}^{s} = \mathrm{T}_{+}^{s}\boldsymbol{b}_{r}^{s}, \quad \text{for } s = 1,\ldots,N, \tag{8}$$
$$\boldsymbol{f}_{1}^{N+1} = M_{\mathrm{ff}}^{N+1,+}\boldsymbol{f}_{\mathrm{r}}^{N} + \mathrm{M}_{\mathrm{fb}}^{N+1,+}\boldsymbol{b}_{\mathrm{r}}^{N}.$$

Applied to the microresonator configurations with one (Section 3) and three (Section 4) inner segments, the above procedure appeared to be unconditionally stable. In principle, the equations allow for different numbers of terms in the mode basis sets on different segments. As in Lohmeyer and Stoffer (2001) the given formulation of the mode expansion algorithm is independent of the light polarization.

3. Simulations of single cavity resonators

For reasons of comparability, all simulations in this paper employ a set of material and geometrical parameters as proposed by Manolatou et al. (1999), with a background refractive index of $n_{\mathrm{b}} = 1.0$, a refractive index of $n_{\mathrm{g}} = 3.2$ for the waveguide cores and the cavity, a gap of $g = 0.29\,\mu\mathrm{m}$ between the waveguides of width $w = 0.2\,\mu\mathrm{m}$ and the square cavity with a sidelength of $W = L = 1.54\,\mu\mathrm{m}$. The calculations are meant for TE polarized light (referring to the naming convention for waveguides with a 1D cross section) with the single component of the electric field being oriented in the y-direction. For the transmission spectra given below, the wavelength interval was restricted to a region where the waveguides are single mode, and where the exciting guided field is confined sufficiently, such that the coupling between the waveguides and the cavity remains weak.

3.1. FREQUENCY RESPONSE

The most noticeable feature in the transmission spectrum is the pronounced resonance, that the mode expansion simulations predict at a wavelength of $\lambda = 1.532\,\mu\mathrm{m}$. Fig. 2 shows the spectral response of the microresonator device in a narrow wavelength interval around this point, and illustrates the electric field pattern at the resonance wavelength.

One can distinguish different contributions to the total electric field. There are outwards traveling waves in the ports C and D of the upper waveguide, and an outwards traveling wave with a slightly larger amplitude in the throughput port B. The electric field in port A is a superposition of the inwards traveling exciting field, and a wave with smaller amplitude that is reflected into the port, hence an inwards traveling wave with a pulsating amplitude. In contrast to the traveling wave patterns that are observed for
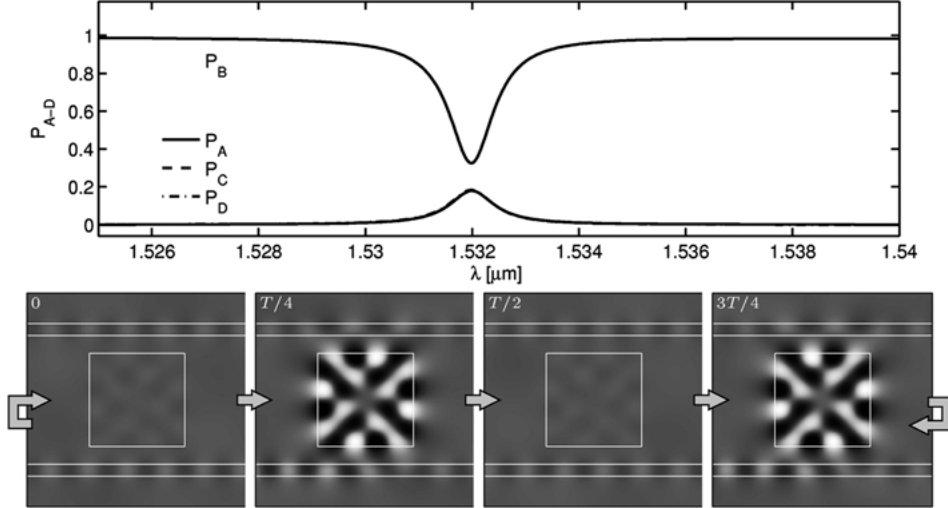
Fig. 2. Top: Relative power transmission P_A to P_D versus the vacuum wavelength, for a resonator as specified by Fig. 1 and the parameters given in the text. The curves for P_A, P_C, and P_D are almost superimposed. Bottom: Snapshots of the electric field at selected timesteps, equidistantly distributed over one time period of $T = 5.11$ fs, for the resonance wavelength $\lambda = 1.532\,\mu$m. The gray scale levels correspond to the y-component of the electric field at the time given in each plot, with the white lines indicating the positions of the waveguide and the cavity in the x–z-plane.

disk- or ring-shaped resonators, the present device shows a standing wave resonance field inside the cavity. This pulsating field pattern does not prefer a direction of propagation, therefore the amounts of power that are dropped into ports C and D and reflected into port A are equal. In the resonant configuration, the cavity region accumulates a maximum electromagnetic energy density which is about 22 times as high as the maximum value in an isolated, equally excited port waveguide.

Given the considerable refractive index contrast, one might try to approximate the field in the cavity by a resonant field on a square domain, enclosed by Dirichlet boundary conditions (Poon *et al.* 2001). Requiring a zero field on the boundary of the square $0 < x < S$, $0 < z < S$, the Helmholtz equation $\partial_x^2 E + \partial_z^2 E + k^2 n_g^2 E = 0$ permits a nonvanishing solution $E(x,z) = E_0(\sin(4\pi x/S)\sin(6\pi z/S) - \sin(6\pi x/S)\sin(4\pi z/S))$ that qualitatively matches the field inside the cavity in Fig. 1, if accompanied by the appropriate time dependence. However, for the resonance to be positioned at $\lambda = 1.532\,\mu$m, one would have to assume a side length of the 'hard' cavity of $S = (4^2 + 6^2)^{1/2}\lambda/2n_g = 1.726\,\mu$m, which is considerably larger than the actual dimension of the 'soft' cavity of $W = 1.54\,\mu$m. Probably a theory that tries to assess the spectral properties of isolated dielectric rectangular cavities would have to consider the open boundary conditions explicitly, at least for the low order resonances which are of interest for the microresonator devices.
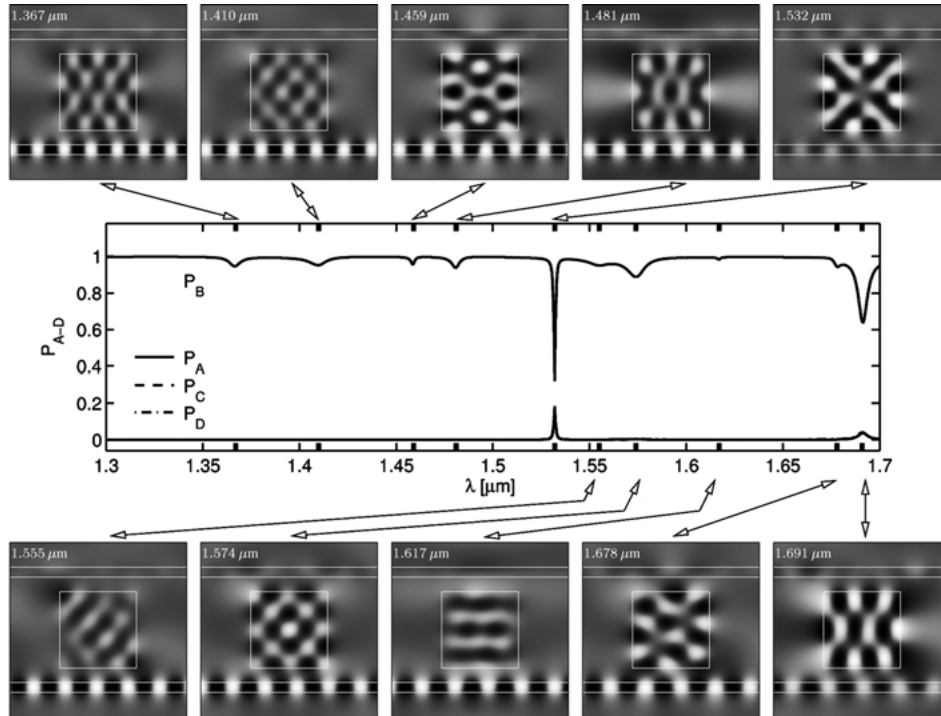
Fig. 3. Spectral response of the square resonator on a wider wavelength interval. The central inset shows the relative power transmission P_A to P_D versus the vacuum wavelength. The upper and lower rows of plots illustrate the stationary electric field at selected time steps, such that the structure of the resonant field becomes visible. The plot parameter is the vacuum wavelength λ of the incoming light.

Here the present mode expansion simulations could serve for benchmarking purposes.

Fig. 3 shows the power transmission and the electric field patterns for several other, less pronounced resonances. All of these exhibit a more or less well defined standing wave pattern inside the cavity. Apart from the resonance at 1.691 µm, there is hardly any power dropped into the upper waveguide.

3.2. INFLUENCE OF PARAMETER SHIFTS

Apart from the estimation of fabrication tolerances, for applications such as the modulation, switching, or routing of a signal, detailed knowledge about the response of the resonator to changes in the material and geometrical parameters is desirable. Fig. 4 summarizes our results for the square cavity.

An alteration of the cavity area (Fig. 4 (a)) has only a minor influence on the shape of the resonance, but a strong influence on its position. A change of 1 nm in the sidelength of the square cavity shifts the resonance by approxi-
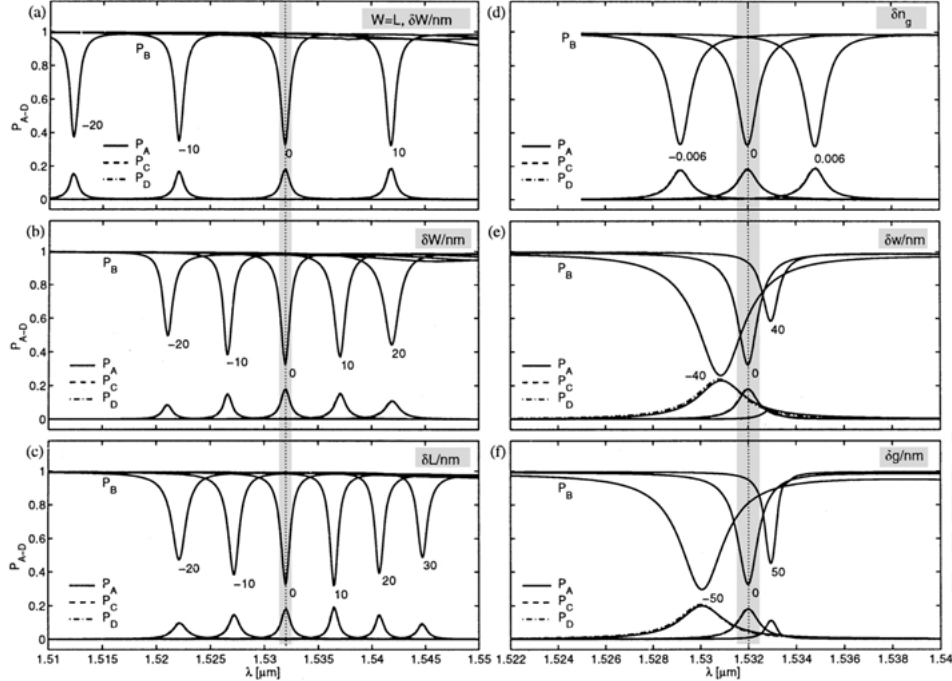
Fig. 4. Relative power transmission P_A to P_D versus the vacuum wavelength λ, for detuned single-cavity resonator configurations. Keeping all other parameters at the values specified in the text, for each plot one quantity q (two in (a)) is changed by small amounts, with the differences δq given as the curve parameters. The altered quantities are the length L and width W of the cavity simultaneously (a), the width W of the cavity (b), the length L of the cavity (c), the refractive index n_g of the guiding regions (d), the width w of the waveguides (e), and the gap g between the waveguides and the cavity (f). The central gray patch indicates the half width of the original resonance curve.

mately the same amount. A similar effect can be achieved by modifying the wavelength of the light inside the cavity, i.e. by changing the refractive index of the cavity material (Fig. 4 (d)). Detuning the resonance position by 1 nm requires to raise or lower n_g by about $2 \cdot 10^{-3}$.

A change in either W or L while keeping the other length fixed (Fig. 4 (b, c)) effects not only a change in the area, but also in the shape of the cavity, with a smaller effect on the resonance position, but a larger effect on the depth of the dip in P_B, when compared to a change in the cavity area. The curves in Fig. 4 (c) suggest that for optimum resonator performance the cavity should be slightly longer than wide ($L > W$), perhaps to compensate for the perturbation of the square symmetry caused by the presence of the waveguides.

Decreasing either the width w of the waveguides (i.e. spreading the guided mode profile), or the gap width g (Fig. 4 (e, f)) strengthens the coupling between the three elements. This has only a small impact on the resonance position, but a pronounced effect on the width and depth of the resonance

peak. A stronger coupling improves the peak resonance level, but at the same time widens the resonance curve.

The finite-difference time-domain (FDTD) simulations (Manolatou *et al.* 1999) locate the resonance at a wavelength of 1.545 µm, which deviates from the present results by an amount that is much larger than the width of the resonance peak. The FDTD results were calculated with a step size of the finite-difference mesh of 20 nm. According to Fig. 4(a), assuming an uncertainty of this order e.g. for the cavity dimensions W and L could well explain the discrepancy in the resonance position.

3.3. SOME REMARKS ON THE CONVERGENCE OF THE MODE EXPANSION APPROXIMATION

The results shown in the previous and in the following sections were computed uniformly on a 10 µm wide computational window, with mode basis sets on all segments that were restricted to 100 terms.

With respect to the width of the computational window, we have checked the convergence of the method for some more pronounced resonances. Doubling simultaneously the window width and the number of terms in the mode expansion, to keep the spectral range of the basis sets, did not lead to any noticeable change of the results on the scale of the given spectra. This indicates that the window width of 10 µm should be adequate for the present structures, despite the sometimes quite pronouncedly radiating cavities.

Fig. 5 shows the wavelength response of the resonator that is predicted by mode expansion simulations with different numbers of terms in the basis sets. If the spectral range of the mode basis is too low, the resonance does not show up at all (20 terms) or it appears to be only shallow and to be located at a wrong position (40 terms). If the number of terms is larger than a certain limit (say 80 terms), a stable convergence establishes; the curves related to 100, 120, and 140 terms are indistinguishable on the scale of the figure.
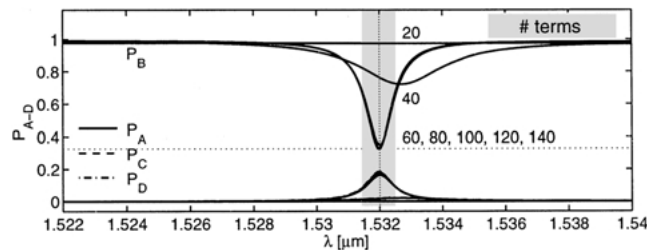

Fig. 5. For the square resonator with parameters as given in the text: relative power transmission P_A to P_D versus the vacuum wavelength λ, as predicted by simulations with different complexity. All calculations use the same computational window $-5\,\mu m \leq x \leq 5\,\mu m$, but a number of terms in the mode expansion that is given as the curve parameter.

On the fixed $10\,\mu$m computational window, the cavity segment (1) supports 18 propagating modes; on segments (0) and (2) only 12 modes are nonevanescent. Obviously including the evanescent modes is essential for correct simulation results. When looking e.g. at the relative amplitudes $|f_m^1|^2$, $|b_m^1|^2$ of the normalized mode fields in the cavity segment, one finds that the evanescent modes receive only small weights. But with a growing number of evanescent terms included, the large amplitudes are shifted among the propagating modes in the cavity segment. In this respect the present simulations differ from investigations of directional couplers or multimode-interference devices by mode expansion techniques, where apparently adequate simulation results can be expected with only a few guided modes included in the basis sets (cf. e.g. Lohmeyer and Stoffer 2001, (to appear)).

4. Filter simulations

With equal amounts of power transferred into both ports of the drop waveguide, the single cavity resonator is not directly suitable for an application as an add-drop filter. This section contains an assessment of a filter device (Manolatou *et al.* 1999), by means of the mode expansion technique. Fig. 6 sketches the relevant geometry, where the two port waveguides are now coupled by two square cavities, spaced by a distance d of $0.72\,\mu$m.
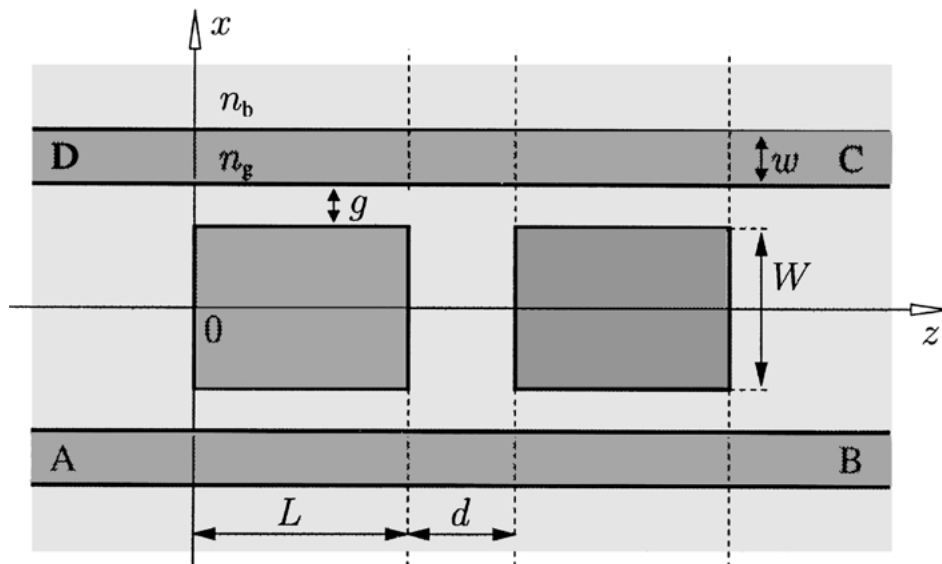

Fig. 6. Add-drop-filter based on two cascaded identical rectangular microresonators. Compared to Fig. 1, only the distance d of the two cavities has to be introduced as an additional parameter.

4.1. FREQUENCY RESPONSE

The spectral response of the filter device in Fig. 7 shows a resonance at the position $\lambda = 1.532\,\mu m$ that was observed also for the single cavity resonator. But in contrast to the simpler device, at that wavelength the throughput port B of the filter receives a relative power of only 3%. Equally low power levels of 2% are reflected into ports A and D, while 68% of the input power is dropped into port C. The resonance has a full width at half maximum (FWHM) of about 1 nm.

The bottom part of Fig. 7 illustrates the electric field pattern at the resonance wavelength. The plots show the electric field at eight nonequidistant points in time, distributed over one period T. The snapshots have been selected to show extremal shapes, where the field either almost cancels in one of the cavities, or where the maximum field levels in the two cavities are approximately equal.

Apparently, the electric field pattern in the cavities can be regarded to be composed of the resonant fields of the single cavities at the same frequency. Assuming that two 'time-domain modes' with opposite symmetry with respect to the line $z = L + d/2$ are excited, each one – apart from signs – with the single cavity field shape inside the squares, one expects a time dependence like
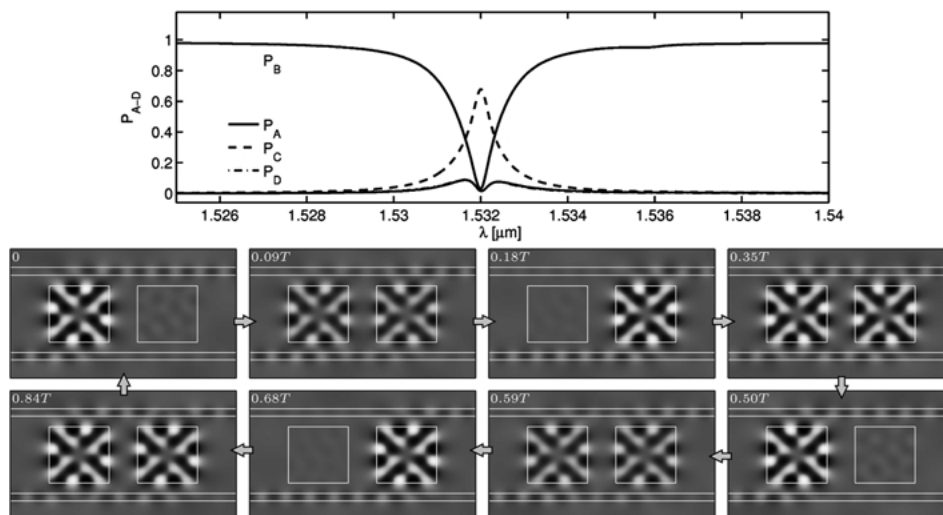

Fig. 7. Top: Relative power transmission P_A to P_D versus the vacuum wavelength, for a filter device as specified by Fig. 6 and the parameters given in the text. The curves for P_A and P_D are almost superimposed. Bottom: Snapshots of the stationary electric field at selected timesteps, nonequidistantly distributed over one period of $T = 5.11$ fs, for the resonance wavelength $\lambda = 1.532\,\mu m$. The gray scale levels correspond to the y-component of the electric field at the time given in each plot, with the white lines indicating the positions of the waveguide and the cavities in the x–z-plane.
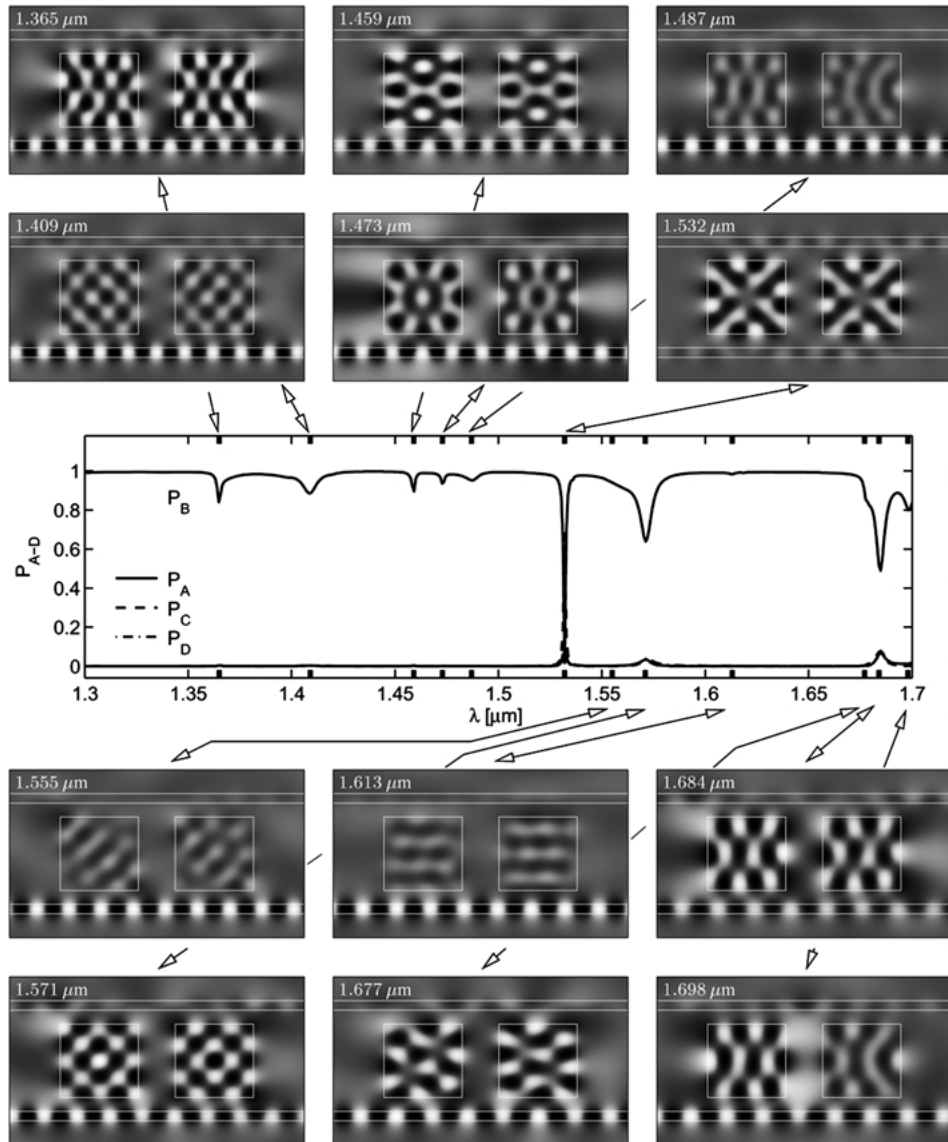
Fig. 8. Spectral response of the filter on a wider wavelength interval. The central inset shows the relative power transmission P_A to P_D versus the vacuum wavelength. The upper and lower rows of plots illustrate the stationary electric field at selected time steps, such that the structure of the resonant field becomes visible. The plot parameter is the vacuum wavelength λ of the incoming light.

$$\begin{pmatrix} E_l \\ E_r \end{pmatrix} = E_0 \left(\begin{pmatrix} 1 \\ 1 \end{pmatrix} \cos(\omega(t - t_0)) + a \begin{pmatrix} 1 \\ -1 \end{pmatrix} \cos(\omega(t - t_0) + \varphi) \right) \qquad (9)$$

for the electric field E_l, E_r in all pairs of corresponding points in the left (1) and right (r) cavity. Here the real quantities a and φ specify the relative

complex amplitude of the antisymmetric time-domain mode with respect to the symmetric one, E_0 is a global amplitude and t_0 is a time offset. The observation that approximately equal maximum field levels are reached in both cavities fixes the relative phase of the two modes to $\varphi \approx \pi/2$. Then one obtains the expression $\Delta t = T \arctan(1/a)/\pi$ for the shorter time interval between zeroes in E_r and E_1; according to Fig. 7 this is a time of $\Delta t = 0.18T$. Hence, apart from proper selection of the time offset, with the assumption of an unequal weighting of the two time-domain modes with $a = 1.6$, Equation (9) reflects qualitatively the time dependence of the electric field inside the filter cavities.

While all resonances of the single cavity resonator show up again in the spectrum of the filter device, these are usually more pronounced, they appear at slightly shifted positions, and they come accompanied by a few additional peaks, which seem to be built from closely neighbored resonances of the single cavities. Fig. 8 is meant to illustrate these observations. Among the resonances the peak at $1.532\,\mu$m is the only one, where a pronounced beating pattern with alternate zeroes in the cavity regions appears, and where channels C and D receive significantly differing amounts of optical power.

The filter performance is to be assessed in terms of the finesse, given by the free spectral range (FSR), divided by the width of the relevant resonance peak. While the FWHM of the resonance at $1.532\,\mu$m was found to be about
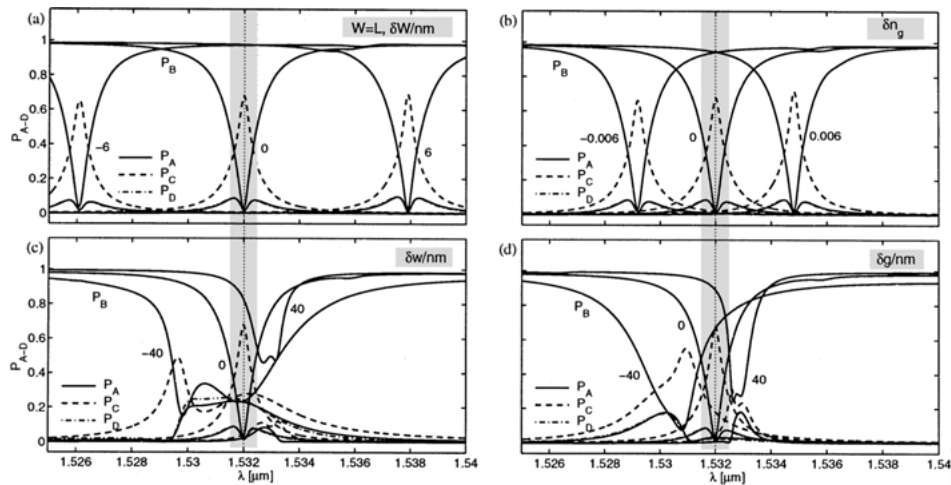

Fig. 9. Relative power transmission P_A to P_D versus the vacuum wavelength λ, for detuned filter configurations. Keeping all other parameters at the values specified in the text, for each plot one quantity q (two in (a)) is changed by small amounts, with the differences δq given as the curve parameters. The altered quantities are (cf. Fig. 6) the width W and length L of the cavity simultaneously (a), the refractive index n_g of the guiding regions (b), the width w of the waveguides (c), and the gap g between the waveguides and the cavities (d).
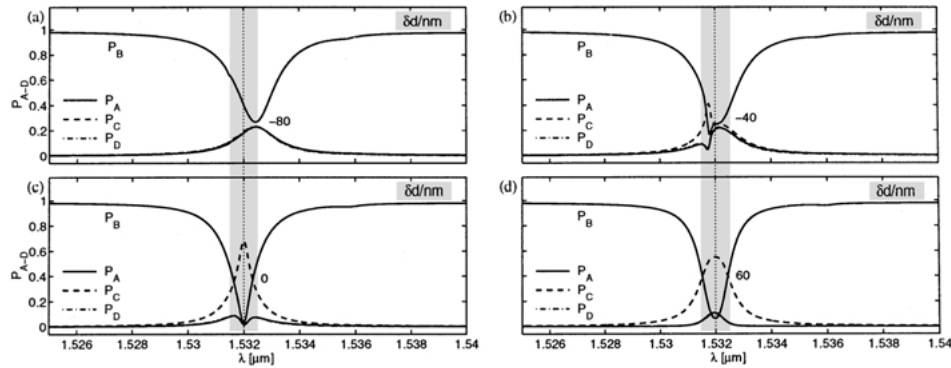
Fig. 10. Relative power transmission P_A to P_D versus the vacuum wavelength λ, for filter devices according to Fig. 6 with differing distances d between the cavity. The curve parameter states the deviation δd from the original value $d = 0.72\,\mu m$; inset (c) shows the original filter curves.

1 nm, the FSR depends on whether one accepts the peak at $1.571\,\mu m$ or that at $1.684\,\mu m$ as the 'next' relevant resonance, leading to finesse values of either 39 or 152.

4.2. INFLUENCE OF PARAMETER SHIFTS

The effect of deviations in the geometrical and material parameters on the filter performance is quite similar to the effect observed for the single cavity resonator. According to Fig. 9, a shift of 1 nm of the resonance position can be achieved alternatively by a change of about 1 nm in the side lengths W and L of the cavities (a), or by altering the cavity refractive index n_g (b) by about $2 \cdot 10^{-3}$. The effect of changes in the parameters w and g, which do not affect the cavities directly, but the strength of the coupling between the cavities and the waveguides, appears to be somewhat puzzling. At least the trend coincides with the single cavity resonator: a weakened coupling, caused either by an enlarged waveguide width or gap width, sharpens the resonance, but also renders it less pronounced.

Similar curve patterns appear, if the spacing d between the cavities is varied, which is probably the most interesting parameter for the filter structure. Fig. 10 shows the results. Apparently, for a properly performing filter a specific phase relation between the waves arriving at the left and at the right cavity is essential, as predicted by the time domain coupled mode theory (Fan et al. 1998; Manolatou et al. 1999). Perturbing this phase relation either by changing the distance between the cavities or by altering the phase velocities of the mediating modes in the waveguides seems to have similar effects.

For given parameters w, g, W, L, n_b, and n_g, we selected the distance d such that a minimum throughput power P_B and a maximum drop level P_C were achieved at the resonance wavelength. This led to the distance $d = 0.72\,\mu\text{m}$, which is significantly smaller than the value of $0.815\,\mu\text{m}$ that was used in the reference FDTD calculations (Manolatou *et al.* 1999). Apart from uncertainties related to the finite difference mesh, the difference of 95 nm in d could explain the discrepancy between the shapes of the filter curves in Fig. 7 and the reference data (Manolatou *et al.* 1999), where the spectrum appears like Fig. 10 (d).

5. Conclusions

Mode expansion simulations allow for a convenient numerical assessment of rectangular integrated optical microresonator devices in two space dimensions. Our calculations confirm the results of the investigations (Manolatou *et al.* 1999) up to the expectable accuracy limits. Being only modestly demanding in terms of computational time and memory consumption, the mode expansion ansatz can replace the involved finite difference time domain calculations, which are usually employed as a reference simulation tool (Li and Liu 1996; Little *et al.* 1997; Manolatou *et al.* 1999).

The technique enables quite rigorous investigations of the spectral response of the resonator units to changes in the various geometrical and material parameters, and it allows for a straightforward extension to the modeling of a sequence of cavities, as it is required for the realization of add-drop-filters.

Considering only 2D structures with somewhat extreme requirements in terms of refractive index contrast and fabrication tolerances, the simulations may be of only small immediate practical interest, although the 2D model could be viewed as a reduction of a realistic device with 3D light confinement by means of effective indices. However, the simulations constitute an efficient numerical complement to a general theory of 'localized states' (Fan *et al.* 1998; Manolatou *et al.* 1999) in the framework of conventional dielectric waveguides.

References

Boriskina, S.V. and A.I. Nosich. *IEEE T. Microw. Theory* **47** 224, 1999.

Chin, M.K. and S.T. Ho. *J Lightwave Technol.* **16** 1433, 1997.

Fan, S., P.R. Villeneuve, J.D. Joannopoulos and H.A. Haus. *Phys. Rev. Lett.* **80** 960, 1998.

Gornik, E. *Science* **280** 1544, 1998.

Li, B.-J. and P.-L. Liu. *IEEE J. Quantum Elect.* **32** 1583, 1996.

Little, B.E., S.T. Chu, H.A. Haus, J. Foresi and J.-P. Laine. *J. Lightwave Technol.* **15** 998, 1997.

Little, B.E., J.-P. Laine and H.A. Haus. *J. Lightwave Technol.* **17** 704–715, 1999.

Lohmeyer, M. and R. Stoffer. *Opt. Quant. Electron.* **33** 413–431, 2001.

Manolatou, C., M.J. Khan, S. Fan, P.R. Villeneuve, H.A. Haus and J.D. Joannopoulos. *IEEE J. Quantum Elect.* **35** 1322, 1999.

Marcatili, E.A.J. *AT&T. Tech. J.* 2103, September 1969.

Nöckel, J.U. and A.D. Stone. *Nature* **385** 45, 1997.

Poon, A.W., F. Courvoisier, and R.K. Chang. 2001, In: *Laser Resonators IV*, eds. A.V. Kudryashov and A.H. Paxton Vol. 4270 (of SPIE Proceedings), pp. 131–138, 2001.

Rowland, D.R. and J.D. Love. *IEE Proc. Pt. J* **140** 177, 1993.

Sztefka, G. and H.P. Nolting. *IEEE Photonic. Tech. L.* **5** 554, 1993.

Vassallo, C. *Optical Waveguide Concepts.* Elsevier, Amsterdam 1991.